

Tomographic Reconstruction of Atmospheric Water Vapor Profiles Using Multi-GNSS Observations

Bence Turák^{1*}, Abir Khaldi¹, Szabolcs Rózsa¹

¹ Department of Geodesy and Surveying, Faculty of Civil Engineering, Budapest University of Technology and Economics, Műegyetem rkp. 3., H-1111 Budapest, Hungary

* Corresponding author, e-mail: turak.bence@emk.bme.hu

Received: 30 May 2022, Accepted: 01 August 2023, Published online: 15 September 2023

Abstract

Continuously operating reference stations (CORS) provide augmentation services for the highly accurate, cm-level GNSS positioning needs of land surveyors, agriculture, and even autonomous vehicles. These stations have accurate coordinates, thus they can be used to estimate the signal delay caused by the neutral atmosphere including the atmospheric water vapor. The estimated zenith wet delay (ZWD) is in a close correlation with the integrated water vapor in the atmospheric column.

Since a ground station tracks several satellites at every epoch, one could also estimate the slant tropospheric delays, which can provide information on the spatial distribution of the atmospheric water vapor, too. This paper introduces a near real-time multi-GNSS processing approach to estimate slant wet tropospheric delays and a coupled tomographic reconstruction technique to estimate the 3D wet refractivity model that can be assimilated in numerical weather models. The estimated zenith tropospheric delays (ZTDs) and tropospheric gradients are used to restore the slant wet delays (SWD) affecting the observed satellite-receiver range. The SWDs are used as input for a tomographic reconstruction algorithm providing the wet refractivities in a pre-defined voxel model. The derived refractivity profiles have been validated with radiosonde observations. The results show that our GNSS tomography approach could reconstruct the refractivities with the uncertainty of 10 ppm below 3 km of altitude and of 0.3 ppm at the altitude of 10 km in terms of standard deviation.

Keywords

GNSS meteorology, tropospheric delay, water vapor

1 Introduction

Atmospheric water vapor (AWV) is extremely important for the Earth's climate. It is a substantial contributor to the natural greenhouse effect and, as a result, provides positive climate feedback in the context of global warming [1–3]. Also, AWV is a critical component of the water cycle and plays a crucial role in energy transport. Evaporated water at lower latitude is transported to higher latitude where it condensates and releases a big amount of heat [4].

The remote sensing of water vapor using the Global Positioning System (GPS) observations was firstly suggested by Bevis et al. [5]. In their paper they explain the theoretical background of the application of tropospheric delays to estimate the integrated water vapor and they introduce the principles of GNSS atmospheric tomography.

The AWV has a complex spatial distribution in the atmosphere. Due to their limited spatio-temporal resolution, traditional atmospheric measurement sensing techniques like radiosonde (RS) and microwave radiometer

(MWR) observations include inaccuracies related to the ongoing spatial and temporal changes in the atmospheric water vapor density [6]. Yao et al. [7] explains that the ultimate solution for an accurate retrieval of AWV with high temporal resolution is the use of GNSS because of its all-weather availability, high accuracy, low cost and long-term stability [7–9]. Traditionally GNSS is capable to retrieve the atmospheric delay caused by the water vapor in the atmospheric column above the receiver, that is closely correlated with the integrated water vapor (IWV). However, the aggregated atmospheric water vapor in the vertical column does not represent the vertical distribution of AWV. To circumvent these drawbacks, the tomographic reconstruction techniques can be used when the refractivities are estimated using the troposphere induced signal delays in the satellite directions [10–12]. These studies suggest also that the reconstructed 3D distribution of water vapor has significantly improved the precipitation forecast.

In this paper, we introduce a near real-time automatic GNSS observation processing facility for meteorological purposes. It processes GNSS observations on an hourly basis and calculates the tropospheric delays and gradients. Furthermore, we also introduce a tomographic reconstruction algorithm that estimates not only the lateral but also the vertical changes of the atmospheric water vapor. The tomographic reconstruction results the 3D model of the refractivity induced by the atmospheric water vapor that could be directly assimilated in some numerical weather models [13].

The paper is organized as follows. First, we briefly introduce the theory of the tropospheric effects on the GNSS signal propagation. Then the developed near-real-time GNSS processing system is discussed in detail providing signal delays in the zenith direction as well as the tropospheric gradients in the north-south and east-west directions accounting for the atmospheric asymmetry in case of weather fronts. Afterwards the tomographic approach is introduced, and a case study is presented using one month of GNSS observations in the Central-Eastern European domain.

2 Tropospheric effects on GNSS positioning

The Global Navigation Satellite Systems (GNSS) provide positioning services using range observations between the receiver and the satellite and calculate the 3D coordinates of the receivers by trilateration. Since the range observation is derived from the travel time of the microwave signals transmitted by the satellite, they tend to be affected by several systematic errors [14]. The observation equation of the phase ranges is:

$$\Phi_k^j = \rho_k^j - c\delta t_k + c\delta t^j + \lambda N_k^j + STD_k^j - I_k^j + v_k^j, \quad (1)$$

where

Φ_k^j is the observed phase range (a partial distance measured by the phase lag between the incoming and the reference signal),

ρ_k^j is the geometrical distance between the satellite and the receiver calculated by the known satellite coordinates and the unknown receiver coordinates,

δt_k the receiver clock error,

δt^j the satellite clock error,

N_k^j the phase ambiguity,

STD_k^j the slant tropospheric delay in the satellite direction,

I_k^j effect of the ionosphere,

v_k^j random observation error,

λ signal wavelength,

c velocity of light in vacuum.

Although the phase range observations are affected by several errors, most of them can be eliminated with the appropriate processing technique. In relative positioning techniques the double differences of the phase range observations are used to estimate the coordinates, which eliminates both the satellite and the receiver clock error. In case of dual-frequency observations one can exploit the frequency dependency of the ionospheric effect and form a so-called ionosphere-free linear combination of the dual frequency observations. Thus, only the tropospheric delays and the phase ambiguities remain as unknowns apart from the stations coordinated in Eq. (1). Integer phase ambiguities can be resolved by several techniques [15–17].

The tropospheric delay heavily depends on the actual atmospheric conditions. Although several empirical models exist to estimate the tropospheric delays [18–21], scientific level GNSS processing software tend to estimate at least a part of the tropospheric delays together with the coordinates.

The tropospheric delay can be split into the hydrostatic and the wet parts. The former one is mostly caused by the atmospheric masses of the dry air. The height of the atmosphere is approximately 50 km and it contains 99% of air mass. Since it is less variable in time and space, it is easier to estimate. The wet part of the delay is caused by the atmospheric water vapor, which is located in the troposphere, the lowest layer of the atmosphere having a thickness of ca. 10 km.

The water vapor content in the stratosphere is close to zero. The wet delay is more variable in both time and space [22, 23] due to the highly variable water vapor distribution. Therefore, precise GNSS positioning techniques account for the hydrostatic part of the delay as a correction, while the wet component is estimated using the GNSS observations.

The tropospheric delay has the magnitude of ca. 2.3 meters in the vertical direction, out of this ca. 90% is caused by the hydrostatic part and 10% is induced by the wet part of the tropospheric masses. In GNSS data processing, these vertical delays are mapped to the satellite directions using an appropriate mapping function:

$$STD = SHD + SWD = ZHD \times m_h(e) + ZWD \times m_w(e), \quad (2)$$

where STD is slant tropospheric delay, SHD is the slant hydrostatic delay, SWD refers to the slant wet delay and $m_h(e)$, $m_w(e)$ are the hydrostatic- and wet mapping functions.

Several types of mapping functions can be used to calculate the tropospheric delays in the satellite directions [24].

These mapping functions were derived from either the standard atmosphere models, radiosonde profiles or even historical numerical weather model analysis. All of them have the limitation to assume that the actual atmospheric conditions can be described by some empirical functions.

Recently, the Department of Geodesy and Geoinformation of the Technical University of Vienna developed an approach to regularly estimate the zenith hydrostatic delays and the mapping function coefficients using the results of numerical weather forecasts. In the VMF1 FC (Vienna Mapping Function 1 – Forecast), the formula given by Niell is used and a part of the coefficients are calculated by ray-tracing the numerical weather forecast models [16, 25, 26].

Thus, the slant delays can be calculated by the following mapping function:

$$m(e) = \frac{1 + \frac{a}{b}}{1 + \frac{1+c}{a}} \cdot \frac{\sin e + \frac{b}{\sin e + c}}{\sin e + \frac{b}{\sin e + c}}, \quad (3)$$

where e is the elevation angle of the satellite at the station, a parameters are estimated using the ECMWF (The European Centre for Medium-Range Weather Forecasts) by the TU Vienna in a global grid for both the hydrostatic and the wet components. The parameters b and c are given, for the wet component they are: $b_w = 0.00146$ and $c_w = 0.04391$.

Although the VMF1 mapping function coefficients are estimated using numerical weather models, the resolution of the global grid is sparse, and the anisotropy of the troposphere is neglected. The tropospheric delay modeling given in Eq. (3) must be extended to account for this anisotropy caused by mainly weather fronts. It assumes that the lateral changes of the tropospheric delay can be described by a tilted plane [16]. By defining the gradients of this plane in two orthogonal directions one can calculate the slant wet delay using the following formula:

$$SWD = ZWD \times m(e) + ZWD \times \frac{\partial m}{\partial e} \times x \times \cos(\alpha) + ZWD \times \frac{\partial m}{\partial e} \times y \times \sin(\alpha), \quad (4)$$

where:

- x tilting parameter in direction North-South
- y tilting parameter in direction East-West
- α azimuth angle from the station to the satellite
- e elevation angle from the station to the satellite

Since the hydrostatic part of the tropospheric delay provides the majority of the effect and is easily estimated as a function of the total air pressure, we use the VMF1 hydrostatic delays as 'a priori' values in the calculations and estimate the wet component of the delay. In view of the fact that many countries have developed their own ground-based augmentation systems for GNSS by establishing networks of continuously operating reference stations, one can even eliminate the coordinate unknowns in Eq. (1) and estimate the wet tropospheric delays after a successful ambiguity resolution of the phase range observations. In the next section such a GNSS data processing facility is introduced.

3 Near real-time GNSS processing system

In the previous section we have discussed the theoretical background of the estimation of tropospheric delays using GNSS observations taken by a network of GNSS receivers. To estimate the tropospheric parameters in near real-time – with the latency of 1–1.5 hours – one needs to use accurate satellite orbits available in near real time. Although the International GNSS Service provides ultra-rapid orbit solutions [27] for this purpose, these products contain GPS orbits only. Fortunately, the Center for Orbit Determination in Europe provides ultra-rapid orbit solutions available for GPS, GLONASS and Galileo [28].

The Bernese V5.2 GNSS processing software is used to automatically pre-process the GNSS observations in hourly batches and to combine the normal equations of the hourly least squares adjustment in the most recent 12 hours to a 12-hour solution. The latter one is used for the estimation of the tropospheric parameters. Since the least squares adjustment technique is sensitive to gross error, special attention must be paid to the careful pre-processing of the phase observations. Moreover, it is important to provide good 'a priori' values for the estimated parameters [16] (Fig. 1).

To eliminate the ionospheric effects, the ionosphere free linear combinations of the double-differenced phase ranges are used in this study. Thus, the observation equations contain only the phase ambiguities, the zenith wet delays and the tropospheric gradient parameters as unknowns. After the successful resolution of the phase ambiguities, the zenith wet delays are estimated. The VMF1 forecast mapping functions are used to map the estimated zenith wet delay to the satellite direction [29].

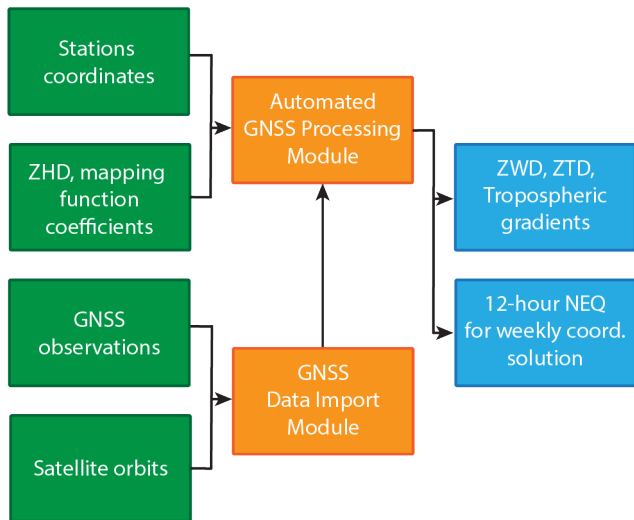


Fig. 1 Tropospheric delay estimation facility

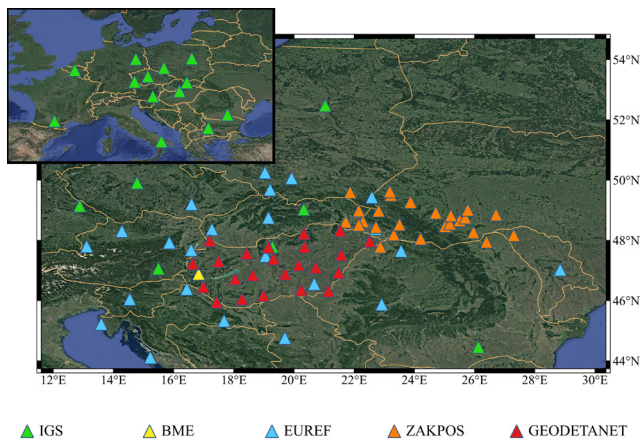


Fig. 2 GNSS stations

Our tropospheric delay estimation relies on several national, and international GNSS networks that contains 87 GNSS stations altogether (Fig. 2):

- IGS,
- EUREF Permanent Network (EPN),
- CORRIGO (a Hungarian GBAS provider),
- BME (stations maintained by the Budapest University of Technology and Economics), and
- ZAKPOS (a GBAS system provider in the Ukraine).

To mitigate the seasonal variation of station positions caused by unmodelled effects, the station coordinates are estimated and fixed on a weekly basis. First, two 12-hour normal equations of every day are combined (UTC 0-11.59 and UTC 12.00-23.59), and a daily coordinate solution is estimated in a separate Bernese process. Second, the daily normal equations of the seven days are combined to obtain the weekly coordinate solution after the end of the GPS week.

The workflow of the hourly GNSS data processing is depicted in Fig. 1 This provides the hourly estimates of ZWDs and respective tropospheric gradients for each station. Tropospheric delay parameters are estimated with hourly temporal resolution and the last but one estimated value is considered as the parameter valid for the respective hour. As an example, we show the ZWDs and the gradients obtained on March 15, 2022, between UTC 16-17:00 in Figs. 3 and 4, respectively.

ZWDs can be assimilated in numerical weather models and are widely used to estimate the integrated water vapor [30], thus this is a valuable observation for the meteorological community.

Tomographic reconstruction is widely used in geophysics [31, 32] and in the engineering practice [33, 34]. Since the slant wet delays can be calculated as a function of the estimated ZWDs and tropospheric gradients, one can apply the tomographic approach for the estimation of the spatial distribution of wet refractivity that can be converted to water vapor densities, when the temperature profiles are known, too.

In the next part of the paper, we introduce the tomographic reconstruction methodology applied for the estimation of the 3D wet refractivity models. First the calculation of the slant wet delays is discussed, then, we briefly

Zenith Wet Delay [m] (2022-03-15_16h_UTC)

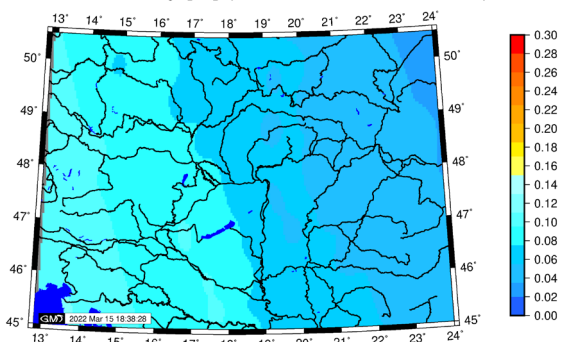


Fig. 3 Map of ZWD values

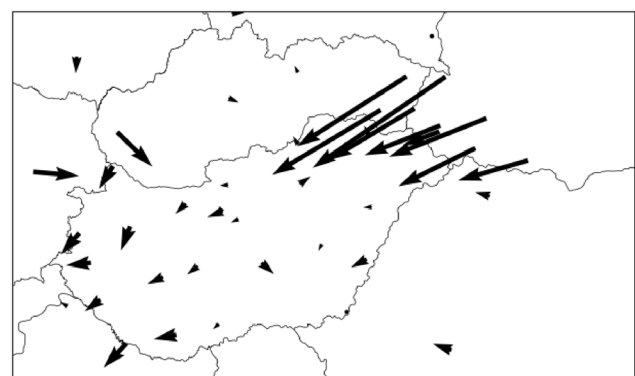


Fig. 4 Tropospheric gradients (dimensionless)

introduce the principles of atmospheric tomography using GNSS, finally the algorithmic realization of the tomographic reconstruction is detailed.

3.1 Restoring slant wet delays

The tropospheric delays in the receiver-satellite direction can be calculated with the integral of the refractivity along the signal propagation path and they can be used to reconstruct the 3D model of atmospheric refractivity by tomographic approaches. Since, the Bernese GNSS software does not provide the slant wet delays (SWD) as an output, [16], we have to firstly restore the SWDs using the ZWDs, the mapping function coefficients and the tropospheric gradient parameters. To keep the consistency with the GNSS processing, we use the same VMF1 mapping function coefficients in the restore step that are used for the estimation of ZWDs in the near real-time processing system (Eq. (3)).

The flow-chart of the tomographic reconstruction algorithm is depicted in Fig. 5. To calculate the SWDs between the receiver and the satellite, the satellite elevation angles and azimuths are calculated at the ground stations for the respective epoch using the GNSS station coordinates and the ultra-rapid satellite orbits. Afterwards, the SWDs are calculated using Eq. (4) based on the estimated ZWDs and tropospheric gradient parameters. The SWDs are calculated for each station and for all the visible GPS, GLONASS and Galileo satellites. These SWDs are used in the next step for the tomographic reconstruction of the atmospheric refractivity field.

3.2 Tomographic reconstruction

We have seen in the previous section that the SWDs along the signal path can be restored from the estimated ZWDs and tropospheric gradient parameters. These SWDs can be used to reconstruct the 3D refractivity field in the atmosphere using the tomographic technique.

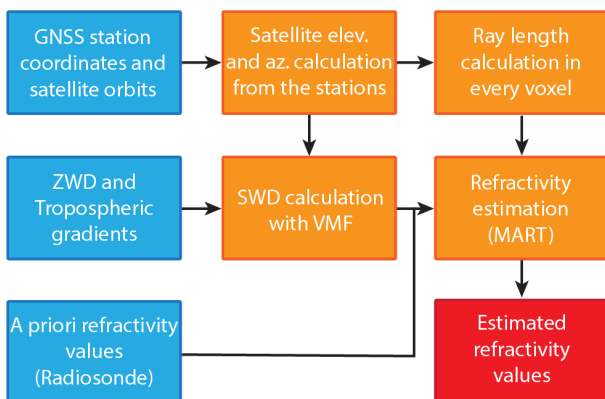


Fig. 5 Tomographic reconstruction algorithm

Tropospheric delays in the satellite direction are defined as the integral of the refractivity along the signal path:

$$STD = \int (n-1) ds = 10^6 \int N ds, \quad (5)$$

where n is the refractive index and N is the refractivity. Below the frequency of 30 GHz, the refractivity (N) can be divided into two parts: the hydrostatic refractivity (N_H) and the wet refractivity (N_w) [35]:

$$N_T = N_H + N_w. \quad (6)$$

Due to Eq. (6) we can separately integrate the hydrostatic and wet refractivity to obtain the SHD and SWD as seen in Eq. (2). Since the hydrostatic refractivity is mostly caused by the dry air and our aim is to estimate the 3D distribution of the water vapor, we can focus on the wet refractivity only. Following Eq. (5) the SWD can be expressed as a line integral of the wet refractivity (n_w) along the signal path:

$$SWD \approx \int (n_w - 1) ds = 10^6 \int N_w ds. \quad (7)$$

Eq. (7) can be applied for the tomographic reconstruction of the wet refractivities based on the available slant wet delays knowing the signal path between the receiver and the satellite. For the numerical solution, a voxel grid defined the study area. Since the receiver and satellite coordinates are known, the path lengths within each voxel can be easily calculated using a flat earth model (Fig. 6) and neglecting the curvature of the ray path. Horváth et al. [36] has proven that the flat earth approximation leads to an error of less than 3% even for low elevation angle satellites. Afterwards, a system of equations can be set up based on Eq. (7) using all the slant wet delays calculated at a single epoch of the near real-time GNSS observations:

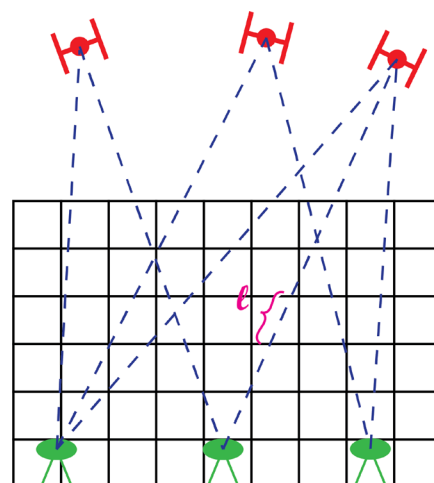


Fig. 6 Schematic grid for the tomographic reconstruction

$$\begin{cases} \sum_{i=1}^n N_w^i l_{1,i} = 10^6 SWD_1 \\ \sum_{i=1}^n N_w^i l_{2,i} = 10^6 SWD_2 \\ \vdots \\ \sum_{i=1}^n N_w^i l_{m,i} = 10^6 SWD_m \end{cases}, \quad (8)$$

where

N_w^i wet refractivity in the voxel i
 $l_{k,i}$ length of the k^{th} ray in voxel i in meter unit
 SWD_k Slant Wet Delay in the k^{th} ray's direction in meter unit

Or in matrix form:

$$\mathbf{Ax} = \mathbf{b}, \quad (9)$$

where

\mathbf{A} is the design matrix containing the path lengths in the voxels:

$$\mathbf{A} = \begin{bmatrix} l_{1,1} & l_{1,2} & \cdots & l_{1,n} \\ l_{2,1} & l_{2,2} & \cdots & l_{2,n} \\ \vdots & \vdots & \ddots & \vdots \\ l_{m,1} & l_{m,2} & \cdots & l_{m,n} \end{bmatrix}, \quad (10)$$

\mathbf{b} is the observation vector containing the estimated SWD values:

$$\mathbf{b} = 10^6 \begin{bmatrix} SWD_1 \\ SWD_2 \\ \vdots \\ SWD_m \end{bmatrix}, \quad (11)$$

and \mathbf{x} is the vector of the unknown wet refractivity parameters:

$$\mathbf{x} = \begin{bmatrix} N_w^1 \\ N_w^2 \\ \vdots \\ N_w^n \end{bmatrix}. \quad (12)$$

Although the number of rays usually exceeds the number of unknowns, the problem can lead to a singular normal equation, since there might be some voxels that have no intersections with the receiver-satellite vectors. To avoid this singularity one can, filter out these voxels and solve the problem using the least squares adjustment technique [37].

In this paper we used a different approach and applied the multiplicative algebraic reconstruction technique (MART) instead. This technique is not sensitive to voxels

without any intersections since it uses an a priori 3D refractivity model and updates only those voxels that have an intersection with any signal path.

In the next section, we briefly introduce the MART technique and its application for GNSS tomography.

3.3 Multiplicative Algebraic Reconstruction Technique

The algebraic reconstruction techniques (ART) are iterative numerical techniques capable solving computational tomography problems [38]. The principle of the ART techniques is that the integral quantities (in our case the SWDs) are calculated using a priori values of the 3D field (the refractivities) and the error in this approximation is applied as a correction to the a priori field values.

The classical ART is not optimal for the reconstruction of the refractivity values since it can provide negative refractivity values. Therefore, we have chosen the multiplicative algebraic reconstruction technique (MART). According to the MART the values of the unknown parameters are calculated according to the following formula:

$$x_k^j = x_{k-1}^j \left(\frac{b_i}{A_i, x} \right)^\theta, \quad k = 1 \rightarrow \infty, \quad (13)$$

where

i refers to the number of the observation,
 j the number of the unknown parameter,
 A_i lengths of the i^{th} ray through the voxels,
 b_i SWD in the direction of the direction of i^{th} ray,
 x Slant Wet Delay in k^{th} ray's direction,
 k is the number of the iterations.
 θ is defined as:

$$\theta = \frac{\lambda A_i^j}{A_i, A_i}, \quad (14)$$

where λ is the relaxation parameter. The convergence of the reconstruction gets faster as λ gets higher. Its default value is 1. The higher λ can provide a solution in fewer iteration steps; on the other hand, the too large λ can cause very big changes which is an overcorrection in the solution. So, the reconstruction will not converge but oscillate around and never provide an appropriate solution.

The iterative algorithm stops when the maximal change in the unknown parameters is less than a predefined threshold:

$$\max_j \left| \frac{x_k^j - x_{k-1}^j}{x_k^j} \right| < \varepsilon, \quad (15)$$

where ε is the threshold.

3.4 Outlier detection and filtering

Since the MART algorithm unlike the least squares adjustment technique does not provide any information on the accuracy of the unknown parameters, one must ensure that no observations affected by blunders are used for the reconstruction. We used two types of outlier filters for the gross error detection. The first approach calculates the linear regression between the original and the reconstructed SWDs and marks those SWDs that do not fit to the regression line. Misfitting shows that the tomographic reconstruction could not resolve these observations, thus they are marked as outliers in the next iteration step.

The drawback of the previous approach is that it neglects the correlation between the uncertainty of the estimated SWDs and the satellite elevation angle. Therefore, another filtering technique was also studied that models the residual error limit as a function of the satellite elevation angle.

These models are introduced in the following subsections in detail.

3.4.1 Regression based outlier filter

The following equation can be used to compute the SWDs using the reconstructed wet refractivity field in order to find outliers in the observations:

$$SWD = Ax \quad (16)$$

Theoretically in an ideal case the calculated **SWD** vector should be the same as the input vector used for the calculation. Thus, comparing the two vectors one should obtain a linear regression relationship which has the gradient of 1 and the offset of 0.

As the measurements are affected by random error, these assumptions are not valid. To find the outlier values, we fitted a linear regression line to the points with a least-squares estimation and created a 3σ band around the fitted line, where σ is the standard deviation of the SWDs' residuals. Those points that are outside this interval are identified as outliers and are removed. We applied this filtering technique on the reconstructed field in a stepwise manner. After the MART technique converged, the outlier detection has been initiated and the outliers were eliminated. Then, the entire process was restarted, and based on the latest reconstructed field, the outlier detection has been repeated. The whole process has been repeated until none of the observations could be identified as outliers.

3.4.2 Outlier filter using pre-defined threshold

The second method that was used for the outlier filtering is based on an elevation angle dependent pre-defined threshold:

$$\text{Threshold}(e) = \frac{t}{\sin(e)}, \quad (17)$$

where

t minimum threshold at the zenith

e elevation angle.

After the tomographic reconstruction was initiated, the SWD values were calculated, just like in Subsection 3.4.1, used the Eq. (16). In an ideal case the reconstructed SWD agrees with the original one. Due to observation error, we observe a residual between the original and the reconstructed SWD. When this residual exceeds the threshold specified by Eq. (17), then the observation is marked as an outlier and it is eliminated from the next iteration. The iterations were repeated until no outlier was detected among the SWDs.

The key of the application of this approach is to find an appropriate minimum threshold value at the zenith. Although one could use the uncertainty stemming from the ZWD estimation during the GNSS data processing, it is well known that the GNSS software tend to underestimate the uncertainties of the calculated ZWD values. Therefore, we have followed a different approach. We used an independent dataset to assess the real accuracy of the estimated ZWD values. According to [39] the uncertainty of the precipitable water vapor (PW) estimated by GNSS is $\sim \pm 1$ mm with respect to results obtained from radiosonde observations. Since the scale factor between PW and ZWD is ca. 6.5, thus the real uncertainty of the estimated ZWDs ca. ± 6.5 mm. Thus, an appropriate threshold of ca. 2 cm for the zenith direction can be calculated using the 3σ rule.

In the next section, we will introduce a case study in which we applied the discussed approach to estimate the 3D refractivity fields using the results of the near real-time GNSS processing facility.

4 Case study

We have already shown that the near real-time GNSS processing system provides ZWDs and tropospheric gradient estimates on an hourly basis for 87 GNSS stations located in Central Europe. To validate our tomographic approach, we used the tropospheric delay estimates in the period

between October 1 and October 31, 2022.

The area of interest is located in Central Europe, covering Hungary, Slovakia and the Eastern part of Ukraine and Romania (Fig. 7).

The predefined voxel boundaries in the latitude, longitude and vertical directions are:

$$\begin{aligned} \varphi &= 45.5^\circ, 46.2^\circ, 46.9^\circ, 47.6^\circ, 48.3^\circ, 49.0^\circ, 49.7^\circ; \\ \lambda &= 15.5^\circ, 17.0^\circ, 18.5^\circ, 20.0^\circ, 21.5^\circ, 23.0^\circ, 24.5^\circ, 26.0^\circ; \\ h &= 0 \text{ km}, 1 \text{ km}, 2 \text{ km}, 3 \text{ km}, 5.5 \text{ km}, 8 \text{ km}, 12 \text{ km}. \end{aligned}$$

After restoring the SWDs from the ZWDs and the gradients according to Eq. (4) these values were preprocessed and only those rays were kept, which has the elevation angle larger than 10° and leave the voxel grid on the top and not on the sides.

Since the MART algorithm requires a priori wet refractivity values for the voxels, we have decided to use the latest radiosonde profile measured at the station 12843 (Budapest) and defined this vertical profile for the whole region as initial values. This enabled us to reinitialize the model in every 12 hours when a new radiosonde observation is made.

Afterwards, the tomographic reconstruction has been done using the approach described in Section 3. We developed a Python program for the whole computation process [40]. We made the tomographic reconstructions for every hour of the study period with updating the a priori refractivity model in every 12 hours using the latest radiosonde profile.

The results of the validation campaign are discussed in the next chapter.

5 Results

The 3D refractivity fields were calculated for each hour in the study period. As an example, we present the reconstructed refractivities for each level obtained on October 19, 2022, at 11UTC in Fig. 8 and Fig. 9 using the

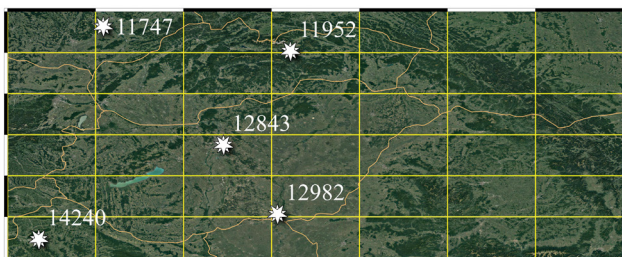


Fig. 7 Voxel grid used for the tomographic reconstruction. Numbers indicate the radiosonde launch sites in the area

regression based and the predefined threshold-based outlier filtering approaches, respectively. The results show that the reconstructed refractivity values follow the general trend along the vertical profile in terms of magnitudes. Moreover, one can observe that there are several voxels, which provide a uniform result close to the edges of the study area. This is caused by the lack of intersecting rays in this part of the area due to the small number of GNSS stations and the fact that the rays leaving the grid on the sides are neglected in the calculations.

As mentioned before, both outlier testing methods were used for the whole study period to be able to compare their performance. The first step of the outlier detection for the given date using the regression-based outlier detection method is shown in Fig. 10.

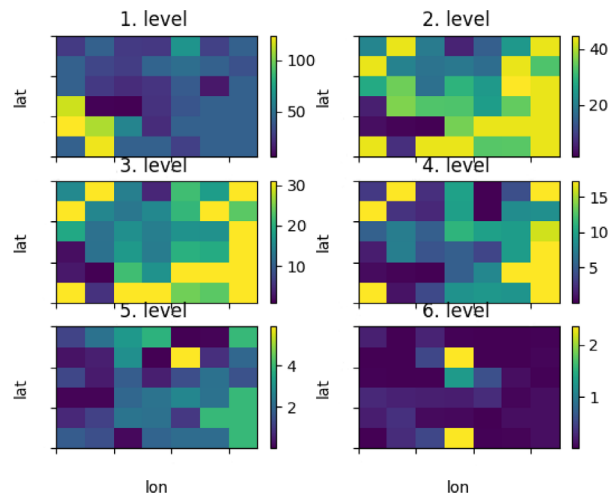


Fig. 8 Estimated wet refractivity field on October 19, 2022, at UTC 11 (regression outlier filter)

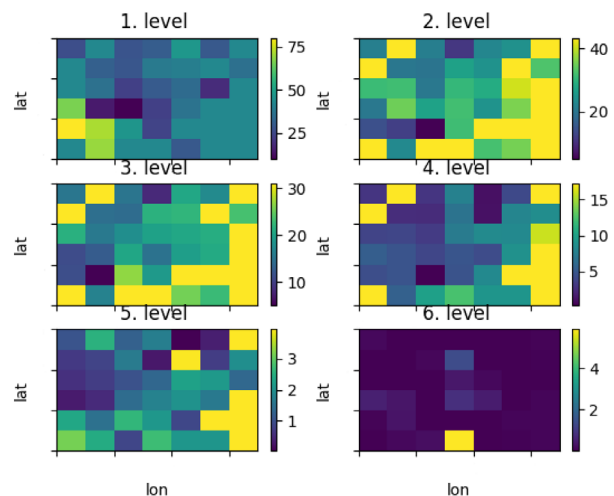


Fig. 9 Estimated wet refractivity field on October 19, 2022, at UTC 11 (threshold outlier filter)

One can clearly see that there are some SWDs that are outside the 3 s band, meaning that they do not fit to the reconstructed field well. These are marked as outliers and are eliminated in the next iteration step.

The result of the linear regression analysis shows that the reconstructed SWD values fit well to the original SWD values after the outliers are detected and removed.

The number of the steps of this iterative outlier detection can be different in every epoch of tomographic reconstruction. In the given epoch, 34 iterations were needed to eliminate all the outliers (Fig. 11).

However, it was already demonstrated that the regression based outlier detection assumes that all of the SWDs have the same accuracy. As a consequence, this method eliminates a substantial amount of rays at the low elevation angles located mainly around the upper part of the

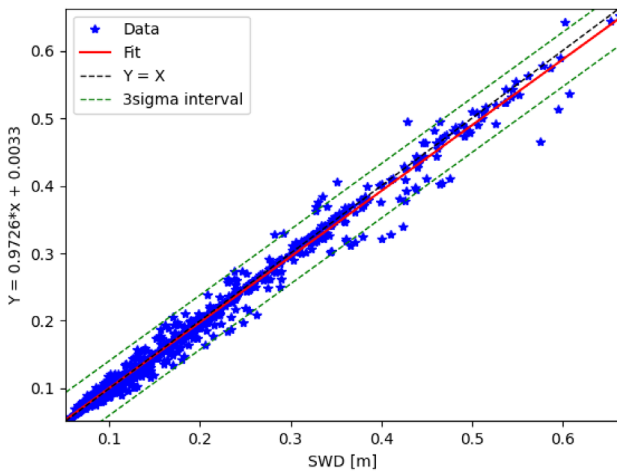


Fig. 10 Regression outlier filter chart on October 19, 2022, at UTC 11 (first filtering step)

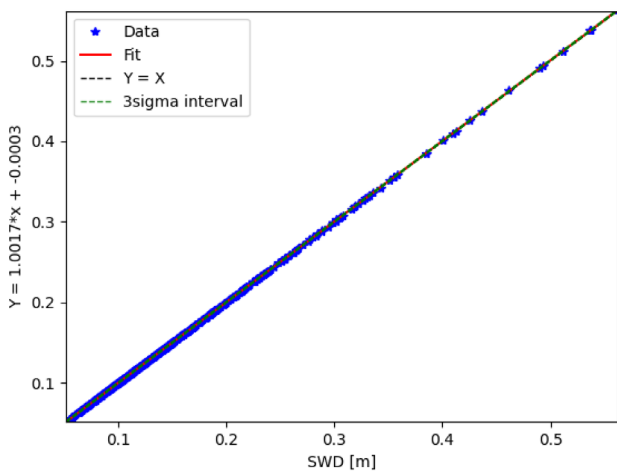


Fig. 11 Regression outlier filter chart on October 19, 2022, at UTC 11 (last filtering step)

regression lines.

Table 1 shows the statistics of the outlier detection (regression method) for all the epochs in the study period. The mean value of the number of rays before the filtering is 923, while after the filtering it is 690. The average rate of the marked and eliminated outlier values is 26% in the study period. This agrees with our assumption that the regression-based outlier detection technique eliminates a substantial amount of rays from the model and lowers its redundancy.

The calculations were repeated using the predefined threshold-based outlier detection method (see Subsection 3.4.2). The residuals of the same reconstruction can be seen in Fig. 12. The outliers marked are denoted with red color on the figure.

It is obvious that significantly less outliers are marked and removed using predefined threshold model leading to a larger redundancy in the model. Moreover, in the second case lower number of repetitions is needed (in this epoch 1 iteration) for the elimination of all the outlier values than in the first (regression based) case. Since, in the second case, the threshold is an unchanging function in every single iteration step, our expectation was only one iteration is enough to eliminate all the outliers. Nonetheless, in some cases, more iteration steps are needed since the reconstruction diverges as the outliers are eliminated.

Table 1 Number of rays before- and after filtering (regression method)

Number of satellites	Before filtering	After filtering	Rate [%]
Minimum	529	279	43
Maximum	1193	1073	97
Mean	922	690	74

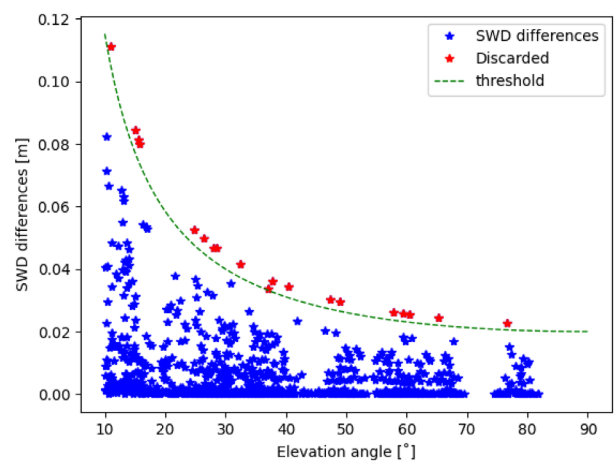


Fig. 12 Threshold outlier filter chart on October 19, 2022, at UTC 11 (first filtering step)

The residual error of the SWDs after the last step of the tomographic reconstruction can be seen in Fig. 13. The figure shows that all of the remaining SWDs fulfill the quality criteria.

Table 2 shows the statistics of the outlier detection (threshold method) for all the epochs in the study period. The mean number of rays before the filtering is 922 and after the filtering is 905. The average rate of the detected and eliminated outlier values is 2%.

The results showed that there is a substantial difference between the rate of the eliminated rays in case of the regression based and the predefined threshold base approaches. We assumed that this phenomenon had an impact on the accuracy of the restored refractivity model, too. To study this impact, the reconstructed wet refractivity values were validated using RS observations. There are five RS stations in our study area (Fig. 7). The wet refractivity profiles were calculated from those RS observations for and compared to the profiles obtained from the reconstructed wet refractivity field using both outlier filtering methods (Fig. 14 and Fig. 15). Since RS observations are also used for the formulation of the a priori refractivity field, we used different RS observations for the formulation of the a priori field and the validation tests. The a priori model was defined always by the radiosonde profile taken 12 hours before the validation epoch. Fig. 14 shows the refractivity profiles recorded at Szeged (WMOID

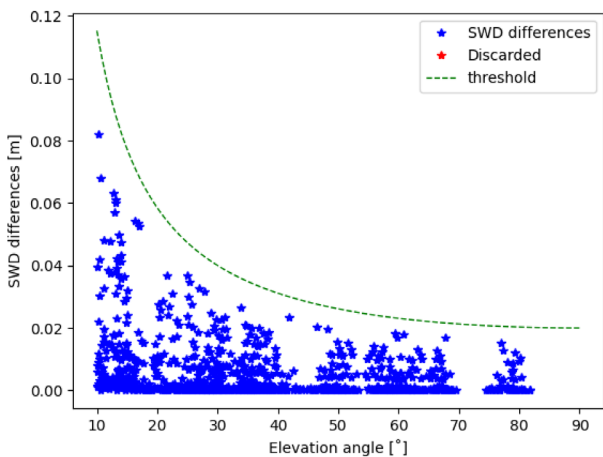


Fig. 13 Threshold outlier filter chart on October 19, 2022, at UTC 11(last filtering step)

Table 2 Number of rays before- and after filtering (threshold method)

Number of satellites	Before filtering	After filtering	Rate [%]
Minimum	529	501	84
Maximum	1193	1191	100
Mean	922	905	98

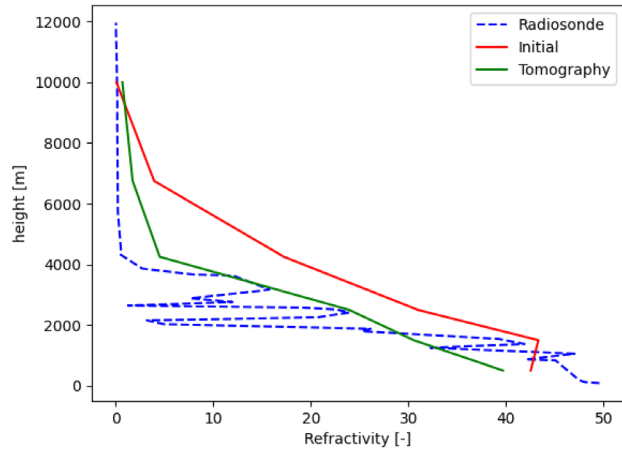


Fig. 14 Wet Refractivity profile at station 12982 (Szeged) 2022-10-19 UTC 11 (regression outlier filtering method)

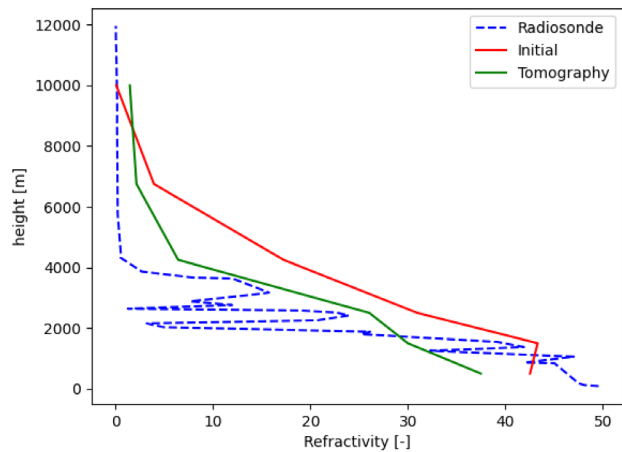


Fig. 15 Wet Refractivity profile at station 12982 (Szeged) 2022-10-19 UTC 11 (threshold outlier filtering method)

12982) using radiosondes and GNSS tomography using the regression outlier method meanwhile Fig. 15 shows the same refractivity profiles from the radiosondes and GNSS tomography using the predefined threshold outlier method as an example. We can observe that the tomographic reconstruction provided a more realistic refractivity profile than the a priori one. However, an underestimation of wet refractivities can be also observed in the lower layers, while an overestimation is present in the upper layers. This can probably be explained by the low vertical resolution of tomography model. Further studies are needed to formulate an optimal voxel model fitted to the spatial distribution of the GNSS stations.

To get an overall picture of the accuracies obtained, we also made these comparisons for all the available RS profiles in the study period. The residual values for Budapest (WMOID 12843) are depicted as a function of altitudes in Fig. 16 and Fig. 17 as an example. The results are as

expected, the lower the altitude, the larger the residual error of the reconstructed refractivity profiles becomes.

The statistics of the computed residuals at each voxel level given in Table 3, while the mean and the standard deviation values are depicted in Fig. 18 and Fig. 19.

The results show that the bias values are not significant for any of the radiosonde stations. One can also observe that the uncertainty of the estimated refractivity values significantly increases closer to the ground. This is also expected since the majority of the atmospheric water vapor is located close to the ground and due to the inversion of atmospheric layers in certain weather conditions makes it difficult to reconstruct the refractivities accurately close to the ground with such a sparse GNSS network. The uncertainty of the wet refractivity values reaches the level of ca. 10 ppm in the voxels in the lower layers. This result agrees well with the results of Trzcina and Rohm [41], who found that the uncertainties change between 5–10 ppm seasonally

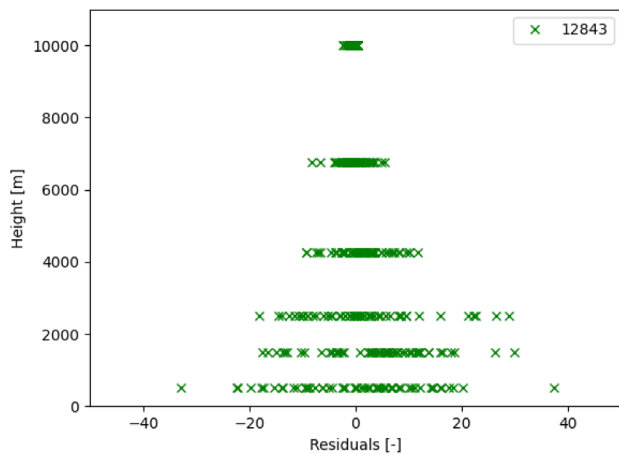


Fig. 16 Residuals at station 12843 (Budapest) in the examined timeframe (2022 October 1-31) (regression outlier filtering method)

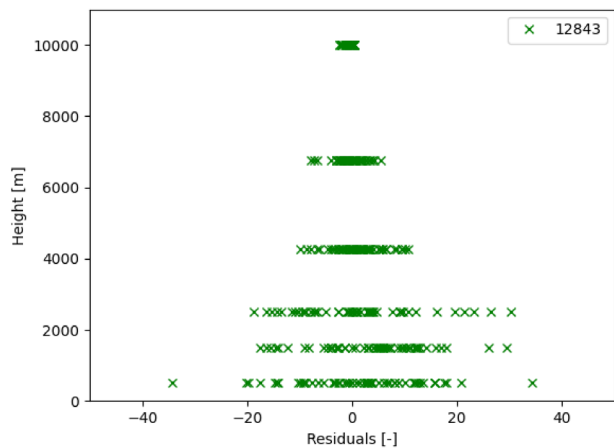


Fig. 17 Residuals at station 12843 (Budapest) in the examined timeframe (2022 October 1-31) (threshold outlier filtering method)

Table 3 Statistical parameters of residuals at every station for each level in both outlier filter cases

Station	Elev. [m]	Min		Max		Mean		Std	
		Regr.	Thre.	Regr.	Thre.	Regr.	Thre.	Regr.	Thre.
11747	500	-14.4	-14.0	20.1	20.1	2.5	2.5	8.4	8.4
	1500	-12.9	-12.9	25.4	25.4	3.4	3.4	10.1	10.0
	2500	-18.0	-17.7	19.5	19.5	0.2	0.3	9.0	8.9
	4250	-6.9	-6.9	6.1	6.1	-1.2	-1.2	3.3	3.3
	6750	-3.6	-3.6	2.4	2.1	-0.3	-0.3	1.4	1.3
	10000	-0.7	-0.7	0.4	0.4	-0.1	-0.1	0.2	0.2
11952	500	-18.0	-18.2	11.6	11.7	-3.6	-3.9	6.3	6.6
	1500	-15.2	-15.1	28.3	18.4	5.5	4.6	7.9	7.1
	2500	-13.1	-13.4	21.7	21.7	1.3	0.8	8.1	8.1
	4250	-11.0	-10.7	11.8	11.8	0.9	0.9	4.0	3.9
	6750	-7.3	-4.6	4.4	4.2	-0.6	0.0	2.5	1.7
	10000	-1.8	-1.4	0.4	0.4	-0.3	-0.2	0.5	0.4
12843	500	-32.8	-34.3	37.4	34.4	0.4	1.4	12.8	12.0
	1500	-17.6	-17.5	29.9	29.4	3.8	3.6	10.2	10.0
	2500	-18.2	-18.7	28.9	30.1	1.3	1.2	10.5	10.9
	4250	-9.3	-10.0	11.7	10.6	1.2	1.1	4.7	4.7
	6750	-6.6	-7.9	5.4	5.4	-0.2	-0.4	2.2	2.5
	10000	-1.5	-2.5	0.5	0.5	-0.2	-0.4	0.5	0.7
12982	500	-16.6	-16.1	21.4	21.3	0.9	0.6	7.8	7.9
	1500	-20.7	-20.9	19.8	19.8	-0.9	-1.1	8.1	8.2
	2500	-21.0	-20.7	29.8	28.9	0.3	0.1	10.6	10.5
	4250	-11.2	-11.0	11.0	12.4	1.4	1.4	4.9	4.8
	6750	-3.2	-3.3	4.1	4.0	0.4	0.4	1.7	1.6
	10000	-1.3	-1.5	0.7	0.7	-0.2	-0.2	0.4	0.5
14240	500	-14.6	-14.6	27.5	27.5	7.7	7.7	8.6	8.6
	1500	-11.5	-11.5	29.9	29.9	3.4	3.4	11.6	11.6
	2500	-17.7	-17.7	25.6	25.6	-0.2	-0.2	10.1	10.1
	4250	-6.3	-6.3	10.7	10.8	0.8	0.8	4.1	4.1
	6750	-3.9	-3.9	3.7	3.6	-0.4	-0.4	1.6	1.6
	10000	-2.1	-2.1	0.8	0.8	-0.3	-0.3	0.6	0.6

up to the level of 2.5 km in terms of standard deviation.

Comparing the statistics of the two filtering methods one can see that there are only minor differences between the uncertainties of the reconstructed refractivities in terms of standard deviation. In some stations and levels, the regression-based outlier filtering method seem to provide better results, while in others the predefined threshold based one. Generally, both methods enable the reconstruction of the refractivity field with the same accuracy level. However, the predefined threshold-based method filters out significantly lower number of rays compared to the regression-based approach. Thus, the risk of forming unpopulated voxels is higher in case of the

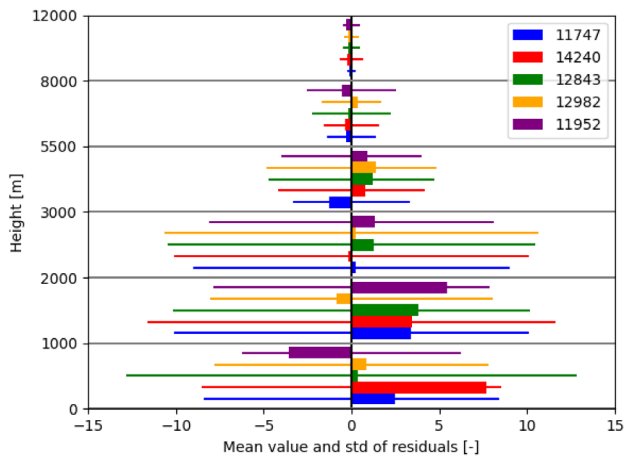


Fig. 18 Mean value (bar) and standard deviation (line) of residuals for each atmospheric layers in the examined timeframe (2022 October 1-31)

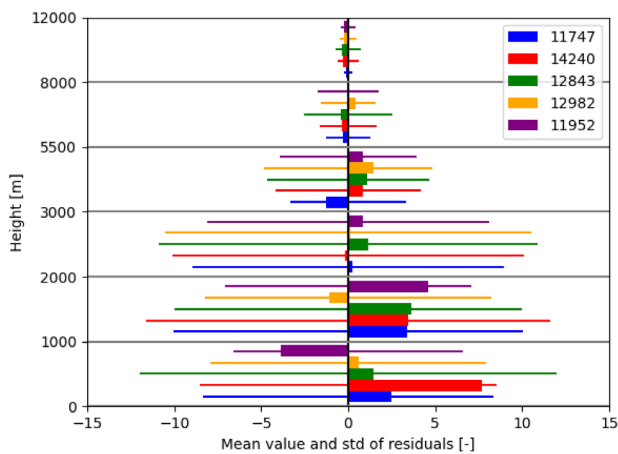


Fig. 19 Mean value (bar) and standard deviation (line) of residuals for each atmospheric layers in the examined timeframe (2022 October 1-31)

regression-based model. Therefore, we propose the application of the predefined threshold approach to filter the outlying slant wet delays in the dataset.

6 Conclusions

A near real-time automatic GNSS data processing system was developed, for the estimation of tropospheric delay parameters for the Carpathian basin with an extension toward Ukraine. The estimated slant wet tropospheric delays were used for the tomographic reconstruction of the 3D model of wet refractivities in the aforementioned area using the slant wet delays stemming from the near real-time GNSS data processing.

To minimize the effect of possible outliers in the calculations, two filtering methods was developed and implemented in the process workflow. One of them uses a regression-based approach to evaluate how well the tomographically reconstructed refractivity field can restore the

original slant wet delays. The other one is based on a pre-defined threshold that takes into consideration the fact that the accuracy of GNSS observations depend on the elevation angle of the tracked satellite. Both methods were applied for a case study in Hungary and the results were validated using radiosonde observations.

The results show that the refractivity profiles could be successfully reconstructed with our approach. The comparison with radiosonde observations did not show any significant bias. The uncertainty of the refractivity values reached the level of 10 ppm for the lower 3 km layer of the atmosphere, while it decreased to 0.3 ppm at the altitude of 10 km during the study period. These results agree well with the ones of Trzcina and Rohm [41]. Although the radiosonde comparisons showed very similar results in case of both filtering methods, the regression-based method eliminated a substantial part of the rays in the model (26%), while the pre-defined threshold-based method kept 98% of the original rays in the model. Since GNSS tomography models are sensitive to the number of rays in the model, we propose to use the filtering method based on the pre-defined threshold to minimize the number of unpopulated voxels in the model.

The algorithms are implemented in a Python software and can be implemented in near real-time applications. This is demonstrated on the GNSS Meteorology website of the Department of Geodesy and Surveying of the Budapest University of Technology and Economics [42].

Acknowledgement

The research reported in this paper is part of project no. BME-NVA-02, implemented with the support provided by the Ministry of Innovation and Technology of Hungary from the National Research, Development and Innovation Fund, financed under the TKP2021 funding scheme. The research has also been funded by the GeoSES - Extension of the operational "Space Emergency System" towards monitoring of dangerous natural and man-made geo-processes in the HU-SK-RO-UA cross-border region EU Interreg+ project (HUSKROUA/1702/8.1/0065).

References

- [1] Mile, M., Benáček, P., Rózsa, S. "The use of GNSS zenith total delays in operational AROME/Hungary 3D-Var over a central European domain", *Atmospheric Measurement Techniques*, 12(3), pp. 1569–1579, 2019.
<https://doi.org/10.5194/amt-12-1569-2019>
- [2] Colman, R. "A comparison of climate feedbacks in general circulation models", *Climate Dynamics*, 20, pp. 865–873, 2003.
<https://doi.org/10.1007/s00382-003-0310-z>
- [3] Colman, R. A. "Climate radiative feedbacks and adjustments at the Earth's surface", *Journal of Geophysical Research: Atmospheres*, 120(8), pp. 3173–3182, 2015.
<https://doi.org/10.1002/2014JD022896>
- [4] Oki, T., Entekhabi, D., Harrold, T. I. "The global water cycle", *The State of the Planet: Frontiers and Challenges in Geophysics*, Volume, 150, pp. 225–237, 2004.
<https://doi.org/10.1029/150GM18>
- [5] Bevis, M., Businger, S., Herring, T. A., Rocken, C., Anthes, R. A., Ware, R. H. "GPS meteorology: remote sensing of atmospheric water vapor using the global positioning system", *Journal of Geophysical Research: Atmospheres*, 97(D14), pp. 15787–15801, 1992.
<https://doi.org/10.1029/92jd01517>
- [6] Wang, H., He, J., Wei, M., Zhang, Z. "Synthesis analysis of one severe convection precipitation event in Jiangsu using ground-based GPS technology", *Atmosphere*, 6, pp. 908–927, 2015.
<https://doi.org/10.3390/atmos6070908>
- [7] Yao, Y., Shan, L., Zhao, Q. "Establishing a method of short-term rainfall forecasting based on GNSS-derived PWV and its application", *Scientific Reports*, 7(1), 12465, 2017.
<https://doi.org/10.1038/s41598-017-12593-z>
- [8] Zhang, Q., Ye, J., Zhang, S., Han, F. "Precipitable Water Vapor Retrieval and Analysis by Multiple Data Sources: Ground-Based GNSS, Radio Occultation, Radiosonde, Microwave Satellite, and NWP Reanalysis Data", *Journal of Sensors*, 2018, 3428303, 2018.
<https://doi.org/10.1155/2018/3428303>
- [9] Rózsa, S., Weidinger, T., Gyöngyösi, A. Z., Kenyeres, A. "The role of GNSS infrastructure in the monitoring of atmospheric water vapor", *Időjárás*, 116(1), pp. 1–20, 2012. [online] Available at: <https://www.met.hu/metadmin/newspaper/2012/03/idojaras-vol116-no1.pdf#page=5>
- [10] Flores, A., Ruffini, G., Rius, A. "4D tropospheric tomography using GPS slant wet delays", *Annales Geophysicae*, 18, pp. 223–234, 2000.
<https://doi.org/10.1007/s00585-000-0223-7>
- [11] Miidla, P., Rannat, K., Uba, P. "Simulated studies of water vapour tomography", [pdf] *WSEAS Transactions on Environment and Development*, 4(3), pp. 181–190, 2008. Available at: <http://www.wseas.us/e-library/transactions/environment/2008/25-861N.pdf>
- [12] Tong, L., Zhang, K., Li, H., Wang, X., Ding, N., Shi, J., Zhu, D., Wu, S. "An Investigation of Near Real-Time Water Vapor Tomography Modeling Using Multi-Source Data", *Journal of Geophysical Research: Atmospheres*, 127(5), 752, 2022.
<https://doi.org/10.3390/atmos13050752>
- [13] Trzcina, E., Hanna, N., Kryza, M., Rohm, W. "TOMOREF Operator for Assimilation of GNSS Tomography Wet Refractivity Fields in WRF DA System", *Journal of Geophysical Research: Atmospheres*, 125(17), e2020JD032451, 2020.
<https://doi.org/10.1029/2020JD032451>
- [14] Teunissen, P. J. G., Montenbruck, O. (eds.) "Springer Handbook of Global Navigation Satellite Systems", Springer, 2017. ISBN: 978-3-030-73172-4
<https://doi.org/10.1007/978-3-319-42928-1>
- [15] Teunissen, P. J. G. "The least-squares ambiguity decorrelation adjustment: method for fast GPS integer ambiguity estimation", *Journal of Geodesy*, 70, pp. 65–82, 1995.
<https://doi.org/10.1007/BF00863419>
- [16] Dach, R., Lutz, S., Walser, P., Fridez, P. (eds.) "Bernese GNSS Software Version 5.2 User manual", University of Bern, Bern Open Publishing, 2015. ISBN: 978-3-906813-05-9
<https://doi.org/10.7892/boris.72297>
- [17] Paláncz, B., Völgyesi, L. "A Numeric-Symbolic Solution of GNSS Phase Ambiguity", *Periodica Polytechnica Civil Engineering*, 64(1), pp. 223–230, 2020.
<https://doi.org/10.3311/PPci.15092>
- [18] Rózsa, S. "Modelling Tropospheric Delays Using the Global Surface Meteorological Parameter Model GPT2", *Periodica Polytechnica Civil Engineering*, 58(4), pp. 301–308, 2014.
<https://doi.org/10.3311/PPci.7267>
- [19] Saastamoinen, J. "Contributions to the theory of atmospheric refraction - part I", *Bulletin Géodésique*, 105(1), pp. 279–298, 1972.
<https://doi.org/10.1007/bf02521844>
- [20] Saastamoinen, J. "Contributions to the theory of atmospheric refraction - part II", *Bulletin Géodésique*, 107, pp. 13–34, 1973.
<https://doi.org/10.1007/bf02522083>
- [21] Niell, A. E. "Global mapping functions for the atmosphere delay at radio wavelengths", *Journal of Geophysical Research: Solid Earth*, 101(B2), pp. 3227–3246, 1996.
<https://doi.org/10.1029/95jb03048>
- [22] Juni, I., Rózsa, S. "Validation of a New Model for the Estimation of Residual Tropospheric Delay Error Under Extreme Weather Conditions", *Periodica Polytechnica Civil Engineering*, 63(1), pp. 121–129, 2019.
<https://doi.org/10.3311/PPci.12132>
- [23] Rózsa, S., Ambrus, B., Juni, I., Ober, P. B., Mile, M. "An advanced residual error model for tropospheric delay estimation", *GPS Solutions*, 24, 103, 2020.
<https://doi.org/10.1007/s10291-020-01017-7>
- [24] Qiu, C., Wang, X., Li, Z., Zhang, S., Li, H., Zhang, J., Yuan, H. "The performance of different mapping functions and gradient models in the determination of slant tropospheric delay", *Remote Sensing*, 12(1), 130, 2020.
<https://doi.org/10.3390/RS12010130>
- [25] "re3data.org: VMF Data Server; editing status 2020-12-14", re3data.org - Registry of Research Data Repositories, 2020.
<https://doi.org/10.17616/R3RD2H>
- [26] Boehm, J., Werl, B., Schuh, H. "Troposphere mapping functions for GPS and very long baseline interferometry from European Centre for Medium-Range Weather Forecasts operational analysis data", *Journal of Geophysical Research: Solid Earth*, 111(2), B02406, 2006.
<https://doi.org/10.1029/2005JB003629>

- [27] Dow, J. M., Neilan, R. E., Rizos, C. "The International GNSS Service in a changing landscape of Global Navigation Satellite Systems", *Journal of Geodesy*, 83, pp. 191–198, 2009.
<https://doi.org/10.1007/s00190-008-0300-3>
- [28] Lutz, S., Beutler, G., Schaer, S., Dach, R., Jäggi, A. "CODE's new ultra-rapid orbit and ERP products for the IGS", *GPS Solutions*, 20(2), pp. 239–250, 2016.
<https://doi.org/10.1007/s10291-014-0432-2>
- [29] Boehm, J., Kouba, J., Schuh, H. "Forecast Vienna mapping functions 1 for real-time analysis of space geodetic observations", *Journal of Geodesy*, 83(5), pp. 397–401, 2009.
<https://doi.org/10.1007/s00190-008-0216-y>
- [30] Juni, I., Rózsa, S. "Developing a global model for the conversion of zenith wet tropospheric delays to integrated water vapour", *Acta Geodaetica et Geophysica*, 53(2), pp. 259–274, 2018.
<https://doi.org/10.1007/s40328-018-0215-2>
- [31] Lo, T., Toksöz, M. N., Xu, S., Wu, R.-S. "Ultrasonic laboratory tests of geophysical tomographic reconstruction", *Geophysics*, 53(7), pp. 947–956, 1988.
<https://doi.org/10.1190/1.1442531>
- [32] Nolet, G. "Seismic tomography", Springer, 1987. ISBN: 978-90-277-2521-9
<https://doi.org/10.1007/978-94-009-3899-1>
- [33] Balázs, G. L., Czoboly, O., Lublós, É., Kapitány, K., Barsi, Á. "Observation of steel fibres in concrete with Computed Tomography", *Construction and Building Materials*, 140, pp. 534–541, 2017.
<https://doi.org/10.1016/j.conbuildmat.2017.02.114>
- [34] Lublós, É., Ambrus, D., Kapitány, K., Barsi, Á. "Air Void Distribution of Asphalts Determined by Computed Tomography", *Periodica Polytechnica Civil Engineering*, 59(4), pp. 503–510, 2015.
<https://doi.org/10.3311/PPci.7608>
- [35] Smith, E. K., Weintraub, S. "The Constants in the Equation for Atmospheric Refractive Index at Radio Frequencies", *Proceedings of the IRE*, 41(8), pp. 1035–1037, 1953.
<https://doi.org/10.1109/JRPROC.1953.274297>
- [36] Horváth, T., Viengdavanh, R., Rózsa, S. "Négydimenziós vízgőz-modellek előállítása GNSS tomográfiával" (Construction of 4D water vapour models by means of GNSS tomography) [pdf] In: *Geomatikai Közlemények*, 17, 2014. pp. 69–78. (in Hungarian) Available at: https://geomatika.epss.hu/storage/volumes/gk_XVII_1.pdf
- [37] Vallyon, J., Horváth, G. "Extended Least Squares LS–SVM", *International Journal of Computational Intelligence*, 3(3), pp. 234–242, 2007.
<https://doi.org/10.5281/zenodo.1071696>
- [38] Bender, M., Dick, G., Ge, M., Deng, Z., Wickert, J., Kahle, H.-G., Raabe, A., Tetzlaff, G. "Development of a GNSS water vapour tomography system using algebraic reconstruction techniques", *Advances in Space Research*, 47(10), pp. 1704–1720, 2011.
<https://doi.org/10.1016/j.asr.2010.05.034>
- [39] Rózsa, S., Khaldi, A., Ács, Á., Turák, B. "Multi-GNSS near real-time precipitable water vapour estimation for severe weather prediction", *Scientific Bulletin of North University Center of Baia Mare*, 35(2), pp. 77–86, 2021.
- [40] Python "GeoPack" [online] Available at: <https://github.com/benceturak/GeoPack>
- [41] Trzcina, E., Rohm, W. "Estimation of 3D wet refractivity by tomography, combining GNSS and NWP data: First results from assimilation of wet refractivity into NWP", *Quarterly Journal of the Royal Meteorological Society*, 145(720), pp. 1034–1051, 2019.
<https://doi.org/10.1002/qj.3475>
- [42] BME "GNSS Meteorology website", Department of Geodesy and Surveying of the Budapest University of Technology and Economics, [online] Available at: <http://gpsmet.agt.bme.hu/>